

The composite-tendency Robert–Asselin–Williams (RAW) filter in semi-implicit integrations

Javier Amezcua* and Paul D. Williams
Department of Meteorology, University of Reading, UK

*Correspondence to: J. Amezcua, Department of Meteorology, University of Reading, Earley Gate, Reading, RG6 6BB, UK.
E-mail: j.AmezcuaEspinosa@reading.ac.uk

Time discretization in weather and climate models introduces truncation errors that limit the accuracy of the simulations. Recent work has yielded a method for reducing the amplitude errors in leap-frog integrations from first-order to fifth-order. This improvement is achieved by replacing the Robert–Asselin filter with the Robert–Asselin–Williams (RAW) filter and using a linear combination of unfiltered and filtered states to compute the tendency term. The purpose of the present article is to apply the composite-tendency RAW-filtered leap-frog scheme to semi-implicit integrations. A theoretical analysis shows that the stability and accuracy are unaffected by the introduction of the implicitly treated mode. The scheme is tested in semi-implicit numerical integrations in both a simple nonlinear stiff system and a medium-complexity atmospheric general circulation model and yields substantial improvements in both cases. We conclude that the composite-tendency RAW-filtered leap-frog scheme is suitable for use in semi-implicit integrations.

Key Words: semi-implicit methods; leap-frog; Robert–Asselin; numerical integration

Received 9 January 2014; Revised 17 March 2014; Accepted 14 April 2014; Published online in Wiley Online Library 17 June 2014

1. Introduction

The performance of time-stepping schemes in atmosphere and ocean models has received increasing attention in recent years (Durran and Blossey, 2012; Clancy and Pudykiewicz, 2013). Arguably, the renewed interest has stemmed from the accumulation of evidence that the errors arising from time discretizations may be a non-negligible component of total model error in weather and climate simulations (Pfeffer *et al.*, 1992; Williamson and Olson, 2003; Mishra *et al.*, 2008; Zhao and Zhong, 2009). The artefacts of time discretization are not limited to the formal accuracy restrictions inflicted by truncation errors (Teixeira *et al.*, 2007) but may also include unexpected effects such as aliasing of Rossby waves (Huang and Pedlosky, 2003) and a loss of stability as the time step is shortened (Heimsund and Berntsen, 2004).

The leap-frog time-differencing scheme is used extensively in current models, in concert with the stabilizing Robert–Asselin filter (Asselin, 1972), to suppress the computational mode (Griffies *et al.*, 2001; Bartello, 2002; Fraedrich *et al.*, 2005; Hartogh *et al.*, 2005; Williams *et al.*, 2009). To increase the amplitude accuracy of this filtered leap-frog scheme, Williams (2009) introduced what has become known as the Robert–Asselin–Williams (RAW) filter. The RAW filter attempts to reduce the filter's impacts on the physical mode by conserving the filter perturbations in an average sense during each application of the filter. Williams (2011) studied the impact of the RAW filter in semi-implicit integrations. Amezcua *et al.* (2011) have found that the RAW filter improves the skill of medium-range weather forecasts compared with the Robert–Asselin filter. Many current

models have subsequently adopted the RAW filter in place of the Robert–Asselin filter (see Williams, 2013 for a list).

Williams (2013) identified two strategies for increasing the amplitude accuracy of the filtered leap-frog scheme further. We recall that the RAW filter eliminates the first-order amplitude errors associated with the Robert–Asselin filter and yields third-order amplitude accuracy. The two improvements proposed by Williams (2013) are as follows. Firstly, leap-frogging over a suitably weighted blend of the filtered and unfiltered tendencies was shown to eliminate the third-order amplitude errors and yield fifth-order amplitude accuracy. Secondly, the use of a more discriminating $(1, -4, 6, -4, 1)$ filter instead of a $(1, -2, 1)$ filter was shown to eliminate the fifth-order amplitude errors and yield seventh-order amplitude accuracy; see Moustauoui *et al.* (2014) for a variant of this approach.

The purpose of the present article is to apply the composite-tendency RAW-filtered leap-frog scheme to semi-implicit integrations. The layout is as follows. Firstly, in the theoretical analysis section, the amplification factor associated with the scheme is derived. Series expansions allow us to derive the asymptotic behaviour of the phase and amplitude errors in the limit of small time steps. Numerical solutions allow us to study the phase and amplitude errors for finite time steps. The stability of the physical and computational modes is studied. Secondly, we test the scheme in semi-implicit integrations of a simple nonlinear stiff system. Finally, we test the scheme in a medium-complexity atmospheric general circulation model, which is closer to the models used for operational numerical weather prediction. The article concludes with a summary and conclusions.

2. Theoretical analysis

2.1. The numerical amplification equation

Consider the two-frequency oscillation equation for the complex variable $x(t)$,

$$\frac{dx}{dt} = i\omega_{low}x + i\omega_{high}x, \tag{1}$$

where ω_{low} and ω_{high} are slow and fast angular frequencies and $i = \sqrt{-1}$ (see e.g. Durran, 1991, 1999). Following Williams (2011), we apply the explicit leap-frog scheme to discretize the ω_{low} term and the implicit Crank–Nicholson scheme to discretize the ω_{high} term. Letting Δt denote the size of the time step and using the RAW filter as a stabilizer, we obtain the following numerical scheme:

$$\frac{x(t + \Delta t) - \bar{\bar{x}}(t - \Delta t)}{2\Delta t} = i\omega_{low}\bar{x}(t) + i\omega_{high}\left[\frac{x(t + \Delta t) + \bar{\bar{x}}(t - \Delta t)}{2}\right], \tag{2}$$

with the RAW filter given by

$$\bar{\bar{x}}(t) = \bar{x}(t) + \frac{\nu\alpha}{2} [\bar{\bar{x}}(t - \Delta t) - 2\bar{x}(t) + x(t + \Delta t)], \tag{3}$$

$$\bar{x}(t + \Delta t) = x(t + \Delta t) + \frac{\nu(\alpha - 1)}{2} [\bar{\bar{x}}(t - \Delta t) - 2\bar{x}(t) + x(t + \Delta t)]. \tag{4}$$

There are two dimensionless parameters in the RAW filter. The first is the usual Robert–Asselin parameter, which satisfies $0 < \nu \ll 1$ and is usually of the order of 10^{-2} – 10^{-1} (see e.g. Asselin, 1972; Déqué and Cariolle, 1986; Durran, 1991). The second is the extra parameter of the RAW filter, which satisfies $0 \leq \alpha \leq 1$ and specifies the relative sizes of the filter perturbations at times t and $t + \Delta t$. In particular, $\alpha = 1$ recovers the classical Robert–Asselin filter.

Following Williams (2013), let us now assume that in a computational code both $x(t)$ and $\bar{x}(t)$ are kept in memory. Then we can use a linear combination of them to calculate the tendency associated with the slow term, which we write as $\gamma\bar{x}(t) + (1 - \gamma)x(t)$. In Williams (2013), the value of γ was restricted to $0 \leq \gamma \leq 1$. This inequality had the purpose of providing an intuitive interpretation to the weights, e.g. 70% of the filtered tendency added to 30% of the unfiltered tendency. This is not necessary, however, for consistency of the scheme. One can write the composite tendency as $x(t) + \gamma(\bar{x}(t) - x(t))$. Then it is evident that there is no restriction on the value of γ and the scheme is consistent, since $\bar{x}(t) \rightarrow x(t)$ as $\Delta t \rightarrow 0$.

Using the composite tendency, one solves for $x(t + \Delta t)$ and Eq. (2) becomes

$$x(t + \Delta t) = \left(\frac{1 + i\Delta t\omega_{high}}{1 - i\Delta t\omega_{high}}\right)\bar{\bar{x}}(t - \Delta t) + \left(\frac{2i\Delta t\omega_{low}}{1 - i\Delta t\omega_{high}}\right)(\gamma\bar{x}(t) + (1 - \gamma)x(t)). \tag{5}$$

We define the complex numerical amplification factor as

$$A = \frac{x(t + \Delta t)}{x(t)} = \frac{\bar{\bar{x}}(t + \Delta t)}{\bar{\bar{x}}(t)} = \frac{\bar{\bar{x}}(t + \Delta t)}{\bar{\bar{x}}(t)}. \tag{6}$$

To find an expression for A , we rewrite Eqs (3)–(5) with x evaluated solely at time t , using Eq. (6). Furthermore, we let

$\omega_{high} = r\omega_{low}$. In particular, we are interested in the case $|r| \geq 1$. A negative r means the slow and fast waves propagate in opposite directions, while a positive r means the direction of both waves is the same. The region $|r| < 1$ is of no practical interest, since it would imply using an explicit scheme for fast oscillations and an implicit scheme for slow oscillations. Nonetheless, $r = 0$ is of interest, since it recovers the single-oscillation case of Williams (2013).

After manipulation, we obtain a homogeneous matrix equation for the vector $[\bar{\bar{x}}(t) \bar{x}(t) x(t)]^T$. For non-trivial solutions, the determinant of the matrix of coefficients must vanish, yielding a cubic equation in A :

$$c_3A^3 + c_2A^2 + c_1A + c_0 = 0, \tag{7}$$

with coefficients given by

$$c_3 = -1 + r i\omega_{low}\Delta t, \tag{8}$$

$$c_2 = \nu + [2 + (\alpha - 1)\gamma\nu] i\omega_{low}\Delta t + (\alpha - 1)\nu r i\omega_{low}\Delta t, \tag{9}$$

$$c_1 = 1 - \nu + [(\alpha - 1)(1 - 2\gamma) - 1] \nu i\omega_{low}\Delta t + (1 - \alpha\nu)r i\omega_{low}\Delta t, \tag{10}$$

$$c_0 = (\alpha - 1)(\gamma - 1)\nu i\omega_{low}\Delta t. \tag{11}$$

These coefficients reduce to those indicated in Williams (2013) when $r = 0$. Equation (7) yields three solutions for $A(i\omega_{low}\Delta t; \nu, \alpha, \gamma, r)$, which we label A_P , A_{C1} and A_{C2} . The first solution is the physical mode, P , and the other two solutions are computational modes, $C1$ and $C2$. One of the computational modes vanishes when $c_0 = 0$, because the cubic equation then reduces to a quadratic equation. This happens if $\gamma = 1$, because then $x(t)$ disappears from Eq. (5), or if $\alpha = 1$ or $\nu = 0$, because then $\bar{\bar{x}}(t) = x(t)$. These conditions are the same as obtained by Williams (2013) for explicit integrations. Therefore, the introduction of the implicitly treated term does not affect the existence of computational modes. For comparison, the exact amplification factor is

$$A_{exact}(\omega_{low}, r) = \exp [i(1 + r)\omega_{low}\Delta t]. \tag{12}$$

For the exact solution, oscillations neither amplify nor dissipate, i.e. $|A_{exact}| = 1$, and the phase advancement per time step is given by $\arg(A_{exact}) = (1 + r)\omega_{low}\Delta t$.

2.2. Asymptotic behaviour

In this section, we will analyze the asymptotic amplitude and phase behaviour of the three modes as $\omega_{low}\Delta t \rightarrow 0$. Let us start with the amplitudes and perform a Maclaurin series expansion for $|A_P|$. The amplitude error for the physical mode is found to be

$$|A_P| - 1 = \frac{\nu(1 - 2\alpha)(1 + r)^2}{2(2 - \nu)}(\omega_{low}\Delta t)^2 + \mathcal{O}[(\omega_{low}\Delta t)^4]. \tag{13}$$

As in Williams (2013), the leading-order amplitude error over one time step is proportional to $(\Delta t)^2$ and is independent of γ . The presence of the fast mode, however, introduces an extra factor of $(1 + r)^2$. Equation (13) is the same as eq. (11) in Williams (2011), in which $\nu \ll 1$ was deliberately ignored in the denominator. If we choose

$$\alpha = \frac{1}{2}, \tag{14}$$

then the coefficient of the quadratic term vanishes. This choice implies using equal and opposite filter perturbations at present

and future times. With this choice, Eq. (13) becomes

$$\begin{aligned} & \left| A_{P, \alpha=1/2} \right| - 1 \\ &= \frac{(1+r)^3 v [(4-v)\gamma - (3+r-v)]}{4(2-v)^2} (\omega_{\text{low}} \Delta t)^4 \\ &+ \mathcal{O}[(\omega_{\text{low}} \Delta t)^6]. \end{aligned} \quad (15)$$

Let us now examine the coefficient of the quartic term. The factor $v/[4(2-v)^2]$ is always positive, since $0 < v < 1$, so the sign of this term is determined by the factor $(1+r)^3[(4-v)\gamma - (3+r-v)]$ and this sign indicates the asymptotic stability of the P mode. In particular, if

$$\gamma = \frac{3+r-v}{4-v}, \quad (16)$$

then this coefficient vanishes and the first non-zero term in the series is proportional to $(\omega_{\text{low}} \Delta t)^6$. For smaller values of γ , the quartic coefficient is negative, indicating asymptotic stability, and for larger values it is positive, indicating asymptotic instability. Comparing Eq. (16) with eq. (18) in Williams (2013), we notice an extra r term in the numerator.

Let us now examine the asymptotic stability of the computational modes. For the sake of brevity, we consider $\alpha = 1/2$ from the beginning. Maclaurin expansions for the magnitudes of C1 and C2 yield

$$\begin{aligned} & \left| A_{C1, \alpha=1/2} \right| = 1 - v + \frac{K(\gamma, v, r)}{8(1-v)^3} (\omega_{\text{low}} \Delta t)^2 \\ &+ \mathcal{O}[(\omega_{\text{low}} \Delta t)^4] \end{aligned} \quad (17)$$

and

$$\left| A_{C2, \alpha=1/2} \right| = \left| \frac{v(\gamma-1)}{2(1-v)} \right| (\omega_{\text{low}} \Delta t) + \mathcal{O}[(\omega_{\text{low}} \Delta t)^3], \quad (18)$$

where the exact expression for $K(\gamma, v, r)$ is spared for brevity. The amplitude of C1 is approximately $1 - v$, indicating unconditional asymptotic stability. The amplitude of C2 is approximately zero, indicating unconditional asymptotic stability. Therefore, both computational modes are stable for small values of $\omega_{\text{low}} \Delta t$.

To complement the preceding amplitude analysis, let us now examine the phase properties of the three modes. We start with a Maclaurin series expansion for $\arg(A_P)$. The first term of the series is $(1+r)\omega_{\text{low}} \Delta t$, which is the phase of the exact amplification factor. After substituting $\alpha = 1/2$, the phase error is found to be

$$\begin{aligned} & \arg(A_{P, \alpha=1/2}) - (1+r)\omega_{\text{low}} \Delta t \\ &= \frac{(r+1)^2(6v\gamma - r(8-v) + 1 - 5v)}{12(2-v)} (\omega_{\text{low}} \Delta t)^3 \\ &+ \mathcal{O}[(\omega_{\text{low}} \Delta t)^5]. \end{aligned} \quad (19)$$

The leading-order phase error is proportional to $(\omega_{\text{low}} \Delta t)^3$, agreeing with Williams (2013). It shows cubic variation with r , agreeing with equation (13) in Williams (2011).

Let us finally analyse the phase properties of the two computational modes. Starting with an expansion for $\arg(A_{C1})$, we obtain

$$\begin{aligned} & \arg(A_{C1, \alpha=1/2}) = \frac{(2-v)(\gamma v + r(1-v) + 1)}{2(1-v)^2} (\omega_{\text{low}} \Delta t) \\ &+ \mathcal{O}[(\omega_{\text{low}} \Delta t)^3]. \end{aligned} \quad (20)$$

The phase advancement of C1 per time step is approximately zero. For $\arg(A_{C2})$, we have

$$\begin{aligned} & \arg(A_{C2, \alpha=1/2}) = S(\gamma, v, r, \omega_{\text{low}} \Delta t) \pi \\ &+ \frac{-(2-v)(\gamma v + r(1-v)) + (3-2v)v}{2(1-v)^2} (\omega_{\text{low}} \Delta t) \\ &+ \mathcal{O}[(\omega_{\text{low}} \Delta t)^3], \end{aligned} \quad (21)$$

where $S = \pm 1$ is a complicated sign function that depends on the parameters of the filter. Hence, the phase advancement of C2 per time step is approximately $\pm \pi$.

2.3. Behaviour for finite $\omega_{\text{low}} \Delta t$

It is of practical interest to study the amplitude and phase behaviour for finite values of $\omega_{\text{low}} \Delta t$. For that reason, we now obtain numerical solutions of Eq. (7). We begin with $|A_P|$, which is a function of $\omega_{\text{low}} \Delta t$ that also depends on the parameters $\{v, \alpha, \gamma, r\}$. We fix $v = 0.1$ for this analysis. In Figure 1, we plot the solutions for different values of α, γ , and r (both positive and negative). Figure 1(b) corresponds to figure 5 of Williams (2009) and Figure 1(k) roughly corresponds to the right panel of figure 6 in Williams (2011).

For all cases, the most dissipative solution corresponds to $\alpha = 1$, the classical Robert–Asselin filter. Note that panels (a) and (c) are the same, since $r = 0$. In the absence of fast oscillations (first row), the solutions for all values of α are very similar for the three values of γ . This is true for the interval studied, $0 \leq \omega_{\text{low}} \Delta t \leq 0.4$, and agrees with figure 4 of Williams (2013). For $r \neq 0$, more apparent differences appear; note that the ordinate range in panels (d)–(l) is one order of magnitude larger than for panels (a)–(c). Let us start with the case $r = \pm 5$ (second row). We see that the amplification for small values of α grows as γ grows. Moreover, the parameter combination $\alpha = 1/2$ and $\gamma = (3+r-v)/(4-v)$ causes $|A_P|$ to remain close to unity for the range of $\omega_{\text{low}} \Delta t$ shown. We notice that the overall behaviour of cases $r = -5$ and $r = 5$ is the same, but for $r = -5$ all the lines remain closer to the ideal $|A_P| = 1$. The difference between positive and negative r becomes less noticeable as we increase $|r|$. The third row of the figure shows the case $r = \pm 10$. The features are very similar to the case $r = \pm 5$, although the growth in amplification/dissipation is slower with respect to $\omega_{\text{low}} \Delta t$. For $r = \pm 100$, the interaction between α and γ is similar and the difference between positive and negative values of r is negligible. In this case, moreover, we infer the existence of a value $0.25 < \alpha < 0.5$ for which $|A_P|$ remains close to unity when $\gamma = (3+r-v)/(4-v)$. Finally, note that the amplification/dissipation of the physical mode saturates for large values of r , as the curves become almost horizontal after some value of $\omega_{\text{low}} \Delta t$.

In Figure 2, we plot the numerical solutions for $|A_{C1}|$ (top row) and $|A_{C2}|$ (bottom row) as functions of $\omega_{\text{low}} \Delta t$. We choose the cases $r = -10$ (dashed lines) and $r = 10$ (solid lines) and fix $v = 0.1$. We use $\gamma = (3-v)/(4-v)$ (left column) and $\gamma = (3+r-v)/(4-v)$ (right column). Different values of α are plotted with different colours. Both modes are stable over the range of $\omega_{\text{low}} \Delta t$ shown, except that mode C1 has a zone of instability when $\alpha = 0$ and $\gamma = (3+r-v)/(4-v)$. Note that $|A_{C2}| = 0$ for $\alpha = 1$, which is expected because this case corresponds to the classical Robert–Asselin filter. For C1, the amplification factor is larger for positive values of r than for negative values of r , regardless of the value of γ . For $r = \pm 10$ this difference is still appreciable, but at larger magnitudes of r this difference tends to disappear (not shown). For C2, the amplification for negative r is smaller than for positive r when $\gamma < 1$, but the opposite happens when $\gamma > 1$. Again, these differences are less noticeable as $|r|$ increases (not shown).

Finally, in Figure 3 we explore the r -dependence of the magnitudes of the three modes; for this purpose we study values in the interval $-1000 \leq r \leq 1000$. We fix $v = 0.1$ and $\alpha = 0.5$ and compare two cases: $\gamma = (3-v)/(4-v)$ (top row) and $\gamma = 1$ (centre row). The latter case corresponds to the classical RAW filter, i.e. with a non-composite tendency, and this case does not have a second computational mode. The bottom row displays the difference of the first minus the second row. As in Williams (2011), we observe that inclusion of the implicitly treated mode stabilizes the numerical scheme and widens the range of frequencies that yield stability. We notice that, under our

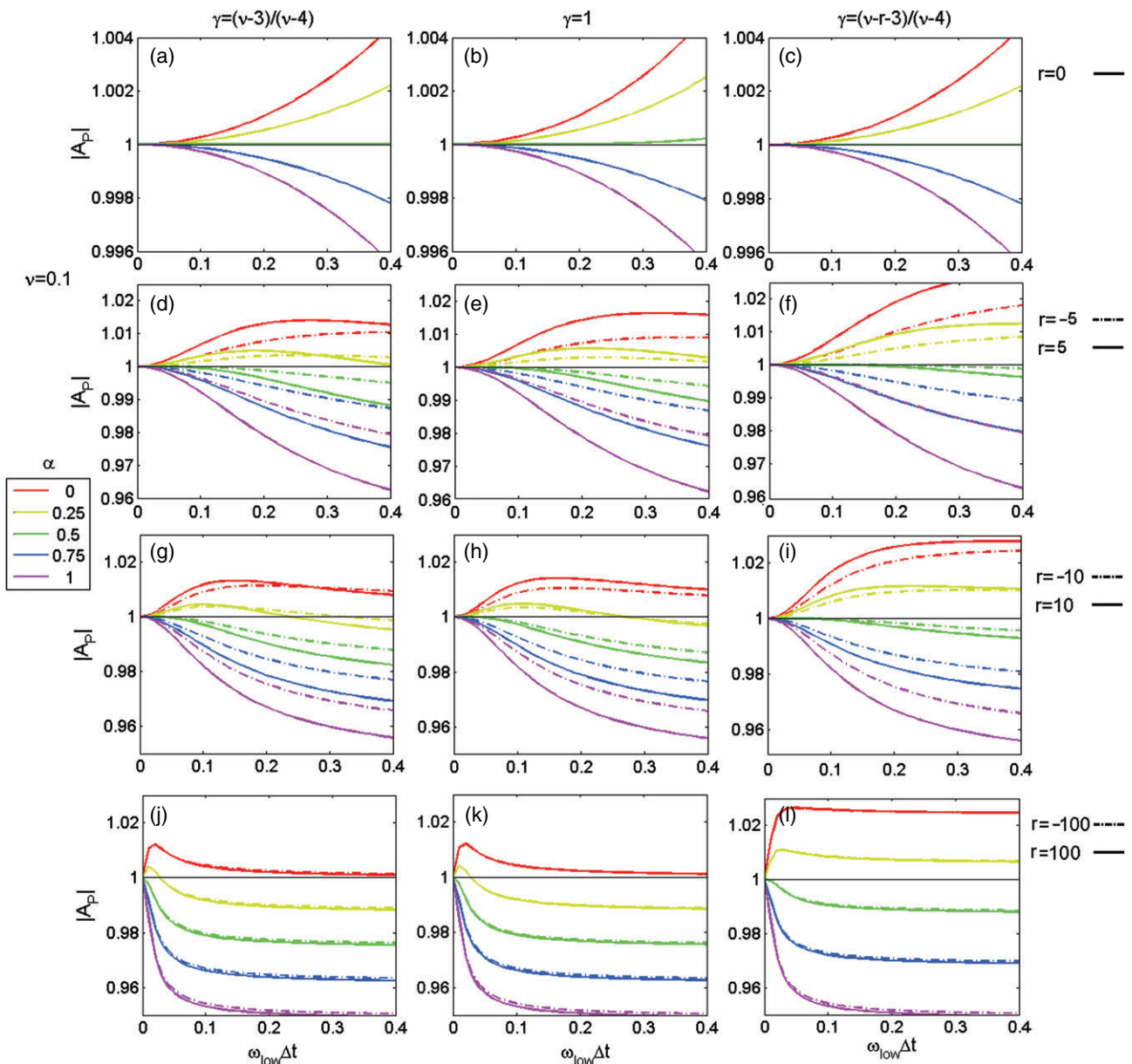


Figure 1. Behaviour of $|A_p|$ as a function of $\omega_{low}\Delta t$ for different values of α (coloured lines), γ (columns) and r (rows). The top row corresponds to $r = 0$, i.e. no fast oscillations and hence no semi-implicit integration. The second row corresponds to $r = -5$ (dashed lines) and $r = 5$ (solid lines), i.e. the fast variable being five times faster than the slow one. The sign of r indicates whether the waves travel in an opposite ($-$) or the same ($+$) direction. The third row corresponds to $r = \pm 10$ and the bottom row corresponds to $r = \pm 100$. The left column corresponds to $\gamma = (3 - \nu)/(4 - \nu)$, i.e. the optimal value found in Williams (2013) for $r = 0$; the middle column corresponds to $\gamma = 1$, i.e. the regular RAW filter; and the right column corresponds to $\gamma = (3 + r - \nu)/(4 - \nu)$, i.e. the value we found to minimize the amplitude error. All panels use $\nu = 0.1$. Note that panels (a) and (c) are identical (since $r = 0$).

choice of α , $|A_p|$ is dissipative. For both values of γ , the damping of this mode increases as both $\omega_{low}\Delta t$ and $|r|$ increase.

The difference plotted in Figure 3(f) shows different behaviour for positive and negative values of r . For $r > 0$ ($r < 0$), the difference is negative (positive), which implies that $|A_{P,\gamma=(3-\nu)/(4-\nu)}|$ is more (less) dissipative than $|A_{P,\gamma=1}|$. The contours corresponding to negative and positive values of the same $|r|$ are not symmetric. The magnitudes of the differences are of the order of 10^{-4} and are concentrated in the region where $|r|$ is small and $\omega_{low}\Delta t$ is large. Figure 3(g) shows a similar behaviour. A vast region of the plane shows negative differences, implying that the computational mode C1 is more damped with $\gamma = (3 - \nu)/(4 - \nu)$ than it is for the regular RAW filter without composite tendency. This is true for the whole region $r > 0$ and for some values of $r < 0$. In contrast, there is a region for small negative values of r and large $\omega_{low}\Delta t$ in which the difference is positive, indicating that $|A_{C1,\gamma=(3-\nu)/(4-\nu)}|$ is more dissipative than $|A_{C1,\gamma=1}|$. Finally, the computational mode C2 exists only when $\gamma \neq 1$ and therefore we only have one plot for this mode, i.e. Figure 3(c). The region where r is small and $\omega_{low}\Delta t$ is large

is particularly important, since the growth of this mode is largest there.

To finish this section, we emphasize that the values of γ obtained in this section are based on the linear equation (1), first in the asymptotic limit $\Delta t \rightarrow 0$ and then under finite time steps. In the next sections, we will be using nonlinear models. One cannot expect these values of γ to be optimal in the nonlinear setting, but they can still be useful as general guidance.

3. Experiments with a simple model

We now test the proposed semi-implicit integration method in a simple yet realistic nonlinear system, the elastic pendulum, following Williams (2011). This stiff system exhibits two modes: a slow rotational mode about the point of suspension and a fast vibrational mode (see e.g. Lynch, 2002). In the present setting, a massless spring of unstretched length $l_0 = 0.63$ m and force constant $k = 100$ N m $^{-1}$ is loaded with a point mass $m = 0.1$ kg subject to a gravitational field $g = 10$ m s $^{-2}$. The equilibrium length of the loaded spring is $l = l_0 + mg/k = 0.64$ m. The two

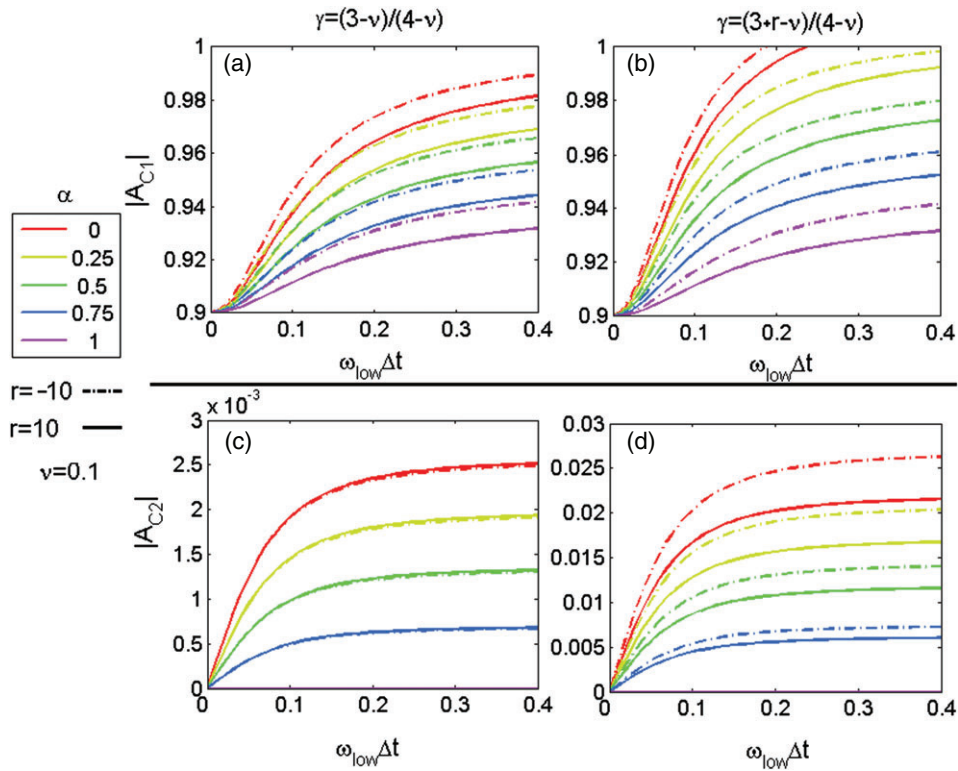


Figure 2. Behaviour of (a, b) $|A_{C1}|$ and (c, d) $|A_{C2}|$ as functions of $\omega_{low} \Delta t$ for different values of α (coloured curves) and for (a, c) $\gamma = (3 - \nu)/(4 - \nu)$ and (b, d) $\gamma = (3 + r - \nu)/(4 - \nu)$. For these plots we have fixed $\nu = 0.1$ and we show the cases $r = -10$ (dashed lines) and $r = 10$ (solid lines).

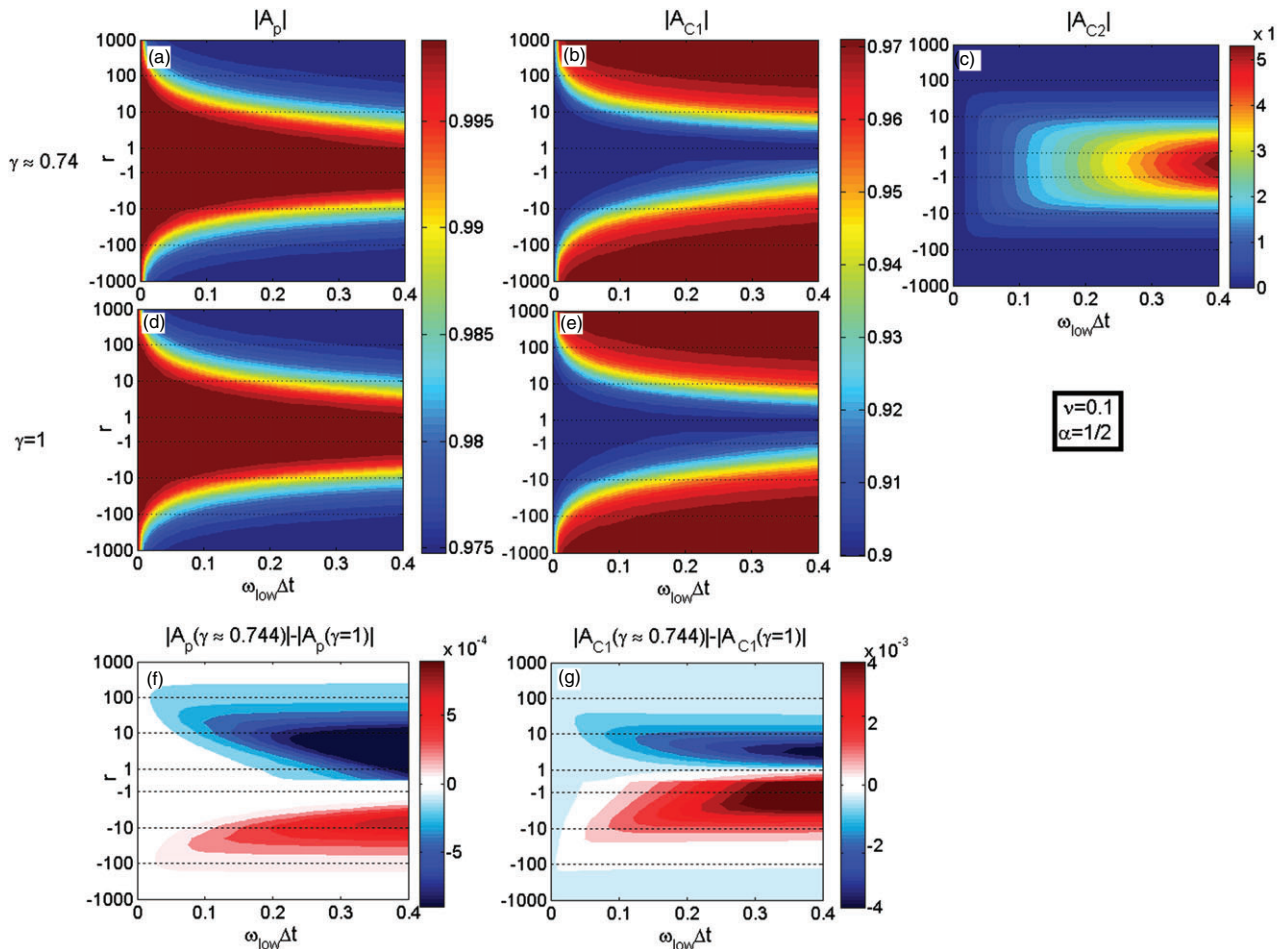


Figure 3. Behaviour of (a, d, f) $|A_p|$, (b, e, g) $|A_{C1}|$ and (c) $|A_{C2}|$ as a function of $\omega_{low} \Delta t$ (horizontal axes) and r (vertical axes). For all panels, $\nu = 0.1$ and $\alpha = 1/2$. Two cases are compared: $\gamma = (3 - \nu)/(4 - \nu)$ (top row) and $\gamma = 1$ (centre row). The differences for $|A_p|$ and $|A_{C1}|$ between the two cases are plotted in the bottom row.

resulting angular frequencies are $\omega_{\text{low}} = \sqrt{g/l} \approx 3.95 \text{ rad s}^{-1}$ and $\omega_{\text{high}} = \sqrt{k/m} \approx 31.62 \text{ rad s}^{-1}$, hence $r = 8$ exactly.

The system is described in polar coordinates by two variables: the polar angle of oscillation with respect to the downward vertical is $\theta(t)$ and the radial coordinate of the point mass is $l(1 + \eta(t))$. The first derivatives of these variables (the velocities) are denoted as $v_\theta(t)$ and v_η . The nonlinear equations of motion are

$$\dot{\theta} = v_\theta, \tag{22}$$

$$\dot{v}_\eta = -\omega_{\text{low}}^2(1 - \cos \theta) - \omega_{\text{high}}^2 \eta + (1 + \eta)v_\theta^2, \tag{23}$$

$$\dot{\eta} = v_\eta, \tag{24}$$

$$\dot{v}_\theta = \frac{-\omega_{\text{low}}^2 \sin \theta - 2v_\theta v_\eta}{1 + \eta}. \tag{25}$$

The underlined terms in these equations are the ones responsible for the fast oscillations and hence they are treated implicitly in the numerical integration. Unusually for a semi-implicit scheme, this system yields explicit analytical expressions for the future state and does not require any iteration. The equilibrium position of this system is $\theta = 0 \text{ rad}$ and $\eta = 0$. The time-continuous equations conserve the total energy

$$E = \frac{1}{2}ml^2[v_\eta^2 + (1 + \eta)^2v_\theta^2] - mgl(1 + \eta) \cos \theta + \frac{1}{2}kl^2(\eta + mg/kl)^2 + mgl - \frac{1}{2}k(l - l_0)^2. \tag{26}$$

For our chosen initial conditions ($\theta = 1$ and $\eta = 0.01$), this corresponds to $E(t = 0) \approx 0.29 \text{ J}$.

The results of our numerical experiments are depicted in Figure 4. The evolution of the slow variable θ is shown in panel (a), that of the fast variable η in panel (b) and that of the energy E in panel (c). We start by computing a reference solution using a fourth-order Runge–Kutta integration scheme with $\Delta t = 10^{-3} \text{ s}$. This can be considered a very good approximation to the exact solution of the system and corresponds to the black lines in Figure 4. This solution conserves energy to within 10^{-10} J at all times during the integration. The integration runs from $t = 0 \text{ s}$ to $t = 10 \text{ s}$, although in the figure we show only $0 < t < 5 \text{ s}$ for clarity.

For the semi-implicit integrations we use $\Delta t = 0.1 \text{ s}$, which is too large to resolve the fast oscillations, but the implicit treatment of the fast mode keeps the integration stable. Setting

$\nu = 0.2$, we compute six solutions. The first uses $\alpha = 1$ and the other five use $\alpha = 1/2$ and $\gamma = \{-3.5, 0, 0.73, 1, 2.79\}$. The case $\alpha = 1$ corresponds to the traditional Robert–Asselin filter and is denoted using grey lines in the figure. This is the most dissipative solution; for both θ and η , the amplitude of the oscillations is reduced with time and therefore the energy decreases with time. The experiments were repeated for $\nu = 0.1$ (figures not shown) with the same qualitative behaviour; the difference is that the effects take longer to be noticeable.

Before describing the results for the different values of γ , it is useful to assess the change in computer time resulting from using a composite tendency in the integration. This model is run in Matlab R2007a and the time for an integration from $t = 0 \text{ s}$ to $t = 10 \text{ s}$ is measured using the tic/toc command. This is repeated 100 times to account for any internal variability in the processing. The average integration time for the standard (pure tendency) RAW-filtered semi-implicit leap-frog scheme is 0.073 s , while the time for the integration using the composite tendency is 0.086 s . This means an increase of 18% in computing time.

Going back to the results of the integration, for $\alpha = 1/2$, the first value we choose is $\gamma = -3.5$ (red line). With this large negative value, $|A_{C2}|$ becomes larger than 1 and therefore the scheme loses stability. As a result, we find that the magnitude of the slow variable grows with time. Consequently, the energy grows with time. Next we choose $\gamma = (3 + r - \nu)/(4 - \nu) \approx 2.79$ (purple line), which is the optimal value for suppressing errors in the P mode (at least according to the linear analysis). The amplitude of the solution decreases with time (although not as fast as in the Robert–Asselin case) and there is a progressive dephasing of the solution. This combination also results in the largest amplitudes for η . Consequently, the energy decreases slowly with time, but not in a smooth manner.

Next, we choose the values $\gamma = 1$ (the traditional RAW filter using the pure filtered tendency, blue line), $\gamma = 0$ (using the pure unfiltered tendency for the RAW filter, yellow line) and $\gamma = (3 - \nu)(4 - \nu) \approx 0.73$ (the optimal value found in Williams (2013) for $r = 0$, green line). The three cases show very similar performance and are much more accurate than the other options. In the three cases, it appears that the amplitude is conserved reasonably well. There is a slight progressive dephasing, which is smallest for the case $\gamma = 0$.

Finally, we take a closer look at the accuracy of the solution for more values of γ . We keep $\alpha = 1/2$ fixed and compute solutions with $\gamma = \{-3.6, -3.55, \dots, 0, \dots, 2.95, 3\}$. For each solution, we compute the root-mean-square error (RMSE) of the energy $E(t)$ with respect to $E(t = 0) \approx 0.299 \text{ J}$ over the whole integration

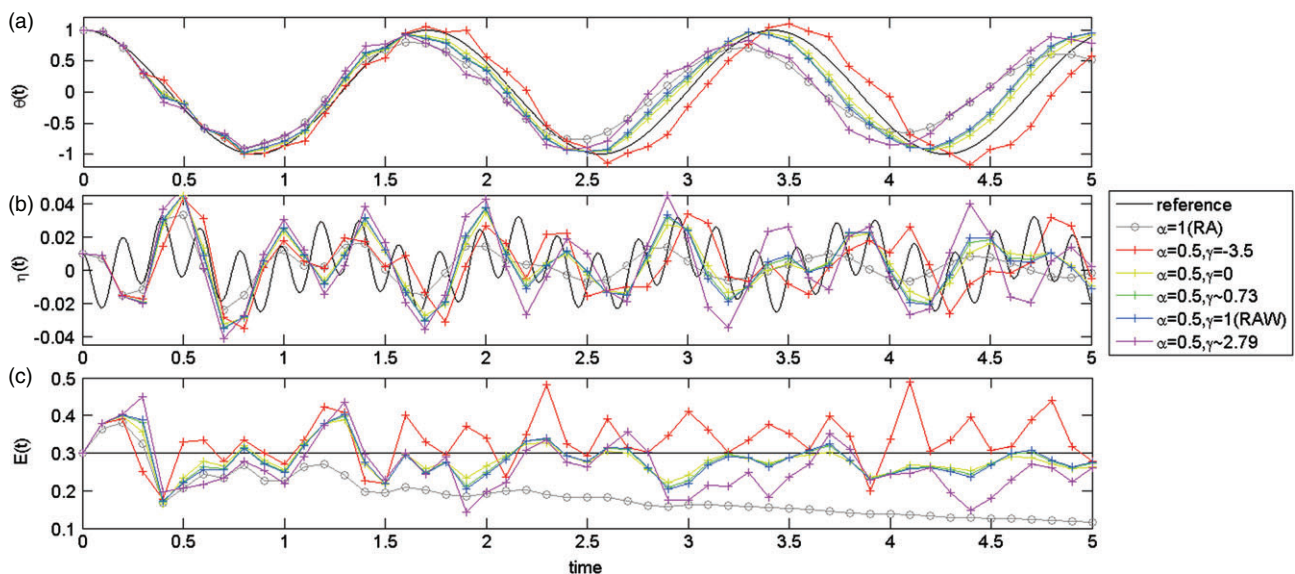


Figure 4. Numerical integration of the nonlinear elastic pendulum equations with initial conditions $\theta = 1 \text{ rad}$, $\eta = 0.01$ and $E_0 \approx 0.299 \text{ J}$. The top row (a) corresponds to the slow variable θ , the middle row (b) to the fast variable η and the bottom row (c) to the energy E . A reference solution using the RK4 scheme with $\Delta t = 0.001$ is shown in black. The other solutions are computed using $\Delta t = 0.1$, $\nu = 0.2$ and different combinations of α and γ .

window. This is done in the following manner:

$$RMSE_E = \sqrt{\frac{1}{N} \sum_{n=1}^N (E(t = n\Delta t) - E_0)^2}, \quad (27)$$

where N corresponds to the total number of time steps up to $t = 10$. The result of this computation is shown in Figure 5. For reference, the RMSE of the solution using the Robert–Asselin filter is 0.181 J. In this figure, it is clear that the RMSE generally grows as $|\gamma|$ grows. There are two local minima in RMSE: the first occurs around $\gamma = -3.2$ and the other around $\gamma = 0.7$. The latter is also the global minimum. It seems that the region $-0.5 < \gamma < 1.5$ is a good choice for this parameter.

We repeat the same experiment for different final values of integration: $t_{\max} = 5, 6, \dots, 30$ s. The result, shown in Figure 6, reveals that the overall shape of Figure 5 appears at about $t_{\max} \approx 7$. As t_{\max} increases, the valley around the negative local minimum of γ becomes narrower. The valley around the positive (and global) minimum of γ is more robust to changes in t_{\max} .

4. Experiments with an AGCM

To finalize this work, we test our numerical integration scheme with a more complicated model, which is closer to the models used for operational numerical weather prediction. As in Amezcua *et al.* (2011), we use the Simplified Parameterizations, primitiveE–Equation Dynamics (SPEEDY) model (Molteni, 2003). SPEEDY

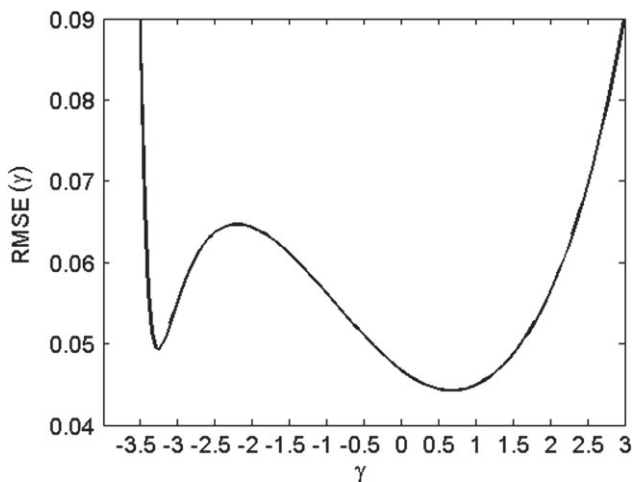


Figure 5. Root-mean-square error in the energy of the solution from $t = 0$ to $t = 10$ s. For the integration, $\nu = 0.2$, $\alpha = 1/2$ and γ is varied (horizontal axis).

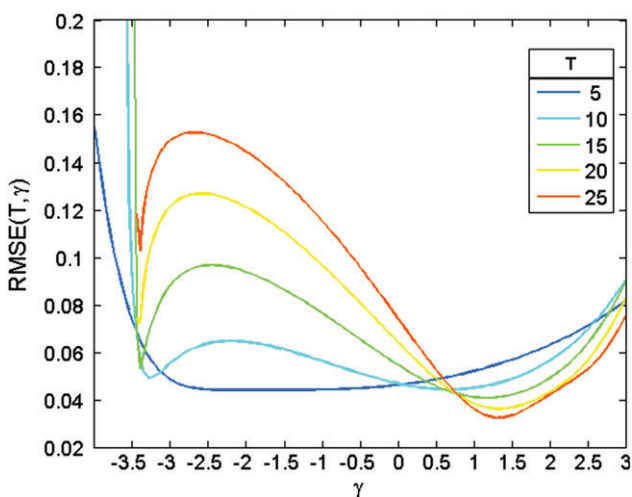


Figure 6. Root-mean-square error in the energy of the solution from $t = 0$ to $t = T$ s. For the integration, $\nu = 0.2$, $\alpha = 1/2$ and γ is varied (horizontal axis). Different values of T are used, represented with different colours.

is a medium-complexity atmospheric general circulation model (AGCM) that has a spectral primitive-equation dynamic core and a set of simplified physical parametrization schemes.

Miyoshi (2005) adapted SPEEDY for use in data assimilation, with output every 6 h. The model time step is 40 min. We use this model implementation in our experiments. It has a resolution of $T30L7$, i.e. with horizontal spectral truncation at total wavenumber 30 and with seven vertical levels. Data are output on a horizontal grid of 96 longitudinal and 48 latitudinal points. The model is based on a spectral dynamical core developed at the Geophysical Fluid Dynamics Laboratory. The model is hydrostatic and is formulated in σ coordinates in the vorticity–divergence form described by Bourke (1974). Five field variables are calculated: zonal wind u , meridional wind v , temperature T , relative humidity q and surface pressure p_s . The geopotential height z for different pressure levels may be obtained by interpolation (since the model is hydrostatic). The description of the basic physical parametrizations can be found in the appendix of Molteni (2003).

For time stepping, SPEEDY uses a Robert–Asselin-filtered leap–frog scheme. The gravity waves are treated implicitly, making this model an ideal setting to test the methods analyzed in this article. Some other schemes (e.g. third-order Adams–Bashforth: Durran, 1991) become unstable under the semi-implicit method and hence are not suited for this model. The Robert–Asselin parameter is selected as $\nu = 0.1$, which has been found to be optimal with this model (Miyoshi, 2005). Moreover, this value lies within the range commonly used in atmospheric models (Williamson, 1983; Déqué and Cariolle, 1986; Durran, 1991).

We will compare three numerical integration settings. The first uses the classical Robert–Asselin filter, the second uses the original RAW filter ($\alpha = 0.53$) and the third uses the composite-tendency RAW filter ($\alpha = 0.53$, $\gamma = 0.73$). This value of α is the one suggested in Williams (2009) and used in Amezcua *et al.* (2011). For γ , in the absence of a well-defined value of r , we use $\gamma = (3 - \nu)/(4 - \nu)$.

Introducing the composite-tendency computation required only a slight modification to the code; only one line needed to be changed in the integration routine. It is necessary, however, to write to disc an extra gridded file (of size 666 kB) with the unfiltered value x_n . This has to be read again in the next integration and is then overwritten.

Again, it is useful to assess the change in computer time when integrating the model with the new method. SPEEDY is coded in Fortran 95 and, in our system, the average time for a 6 h integration of the SPEEDY model using the RAW filter is 0.28 s. When using the composite tendency, this time changes to 0.46 s. This is an increase of 65% and includes writing and reading an extra gridded file every time step and computing the tendency twice.

To assess any possible accuracy improvement in the integration, we use the Anomaly Correlation Coefficient (ACC) for h hour forecasts. The ACC measures agreement between the spatial variations in the forecast and the analysis, each with respect to the climatology. It is calculated as

$$ACC = \frac{\sum_{n=1}^N [(f_n - cs_n)(a_n - cr_n) \cos \phi_n]}{\sqrt{\sum_{n=1}^N [(f_n - cs_n) \cos \phi_n]^2 \sum_{n=1}^N [(a_n - cr_n) \cos \phi_n]^2}}, \quad (28)$$

where f_n is the forecast, a_n is the analysis, cr_n is the climatology of the reanalysis, cs_n is the climatology of the SPEEDY model, ϕ_n is the latitude and N is the total number of grid points for the variable. The subscript labels the points on the grid. The forecasts are initialized from the corresponding reanalysis values.

The ACC is computed for the month of January 1982 every 6 h and then a time average is taken, denoted as \overline{ACC} . For the analysis data, we use the National Centers for Environmental Prediction

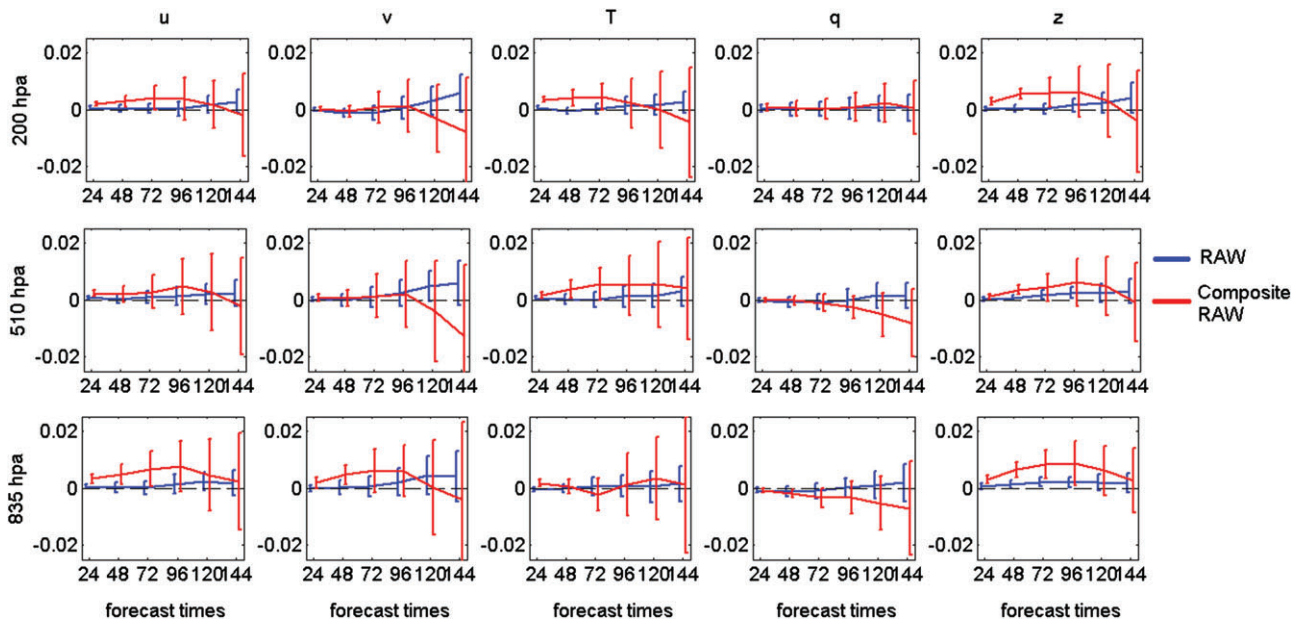


Figure 7. Anomaly correlation coefficient difference with respect to the Robert–Asselin filter for the original RAW filter (blue line) and the composite-tendency RAW filter (red line) for all variables. ACCs are computed at six different forecast times (hours), globally, at three different pressure levels (rows). The bars indicate one standard deviation.

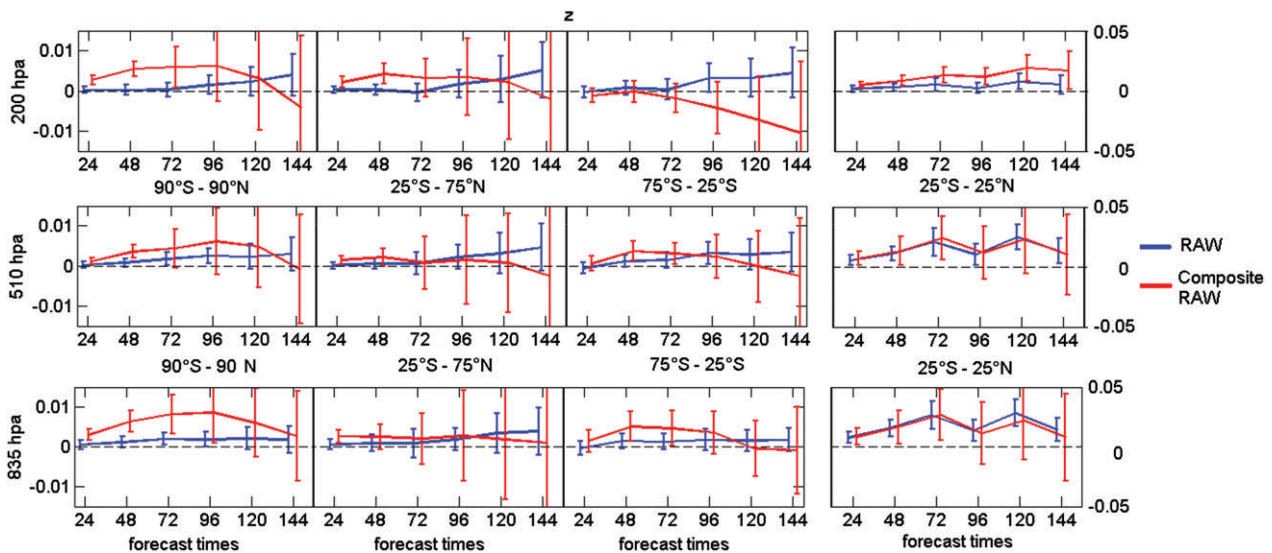


Figure 8. Anomaly correlation coefficient difference with respect to the Robert–Asselin filter for the original RAW filter (blue line) and the composite-tendency RAW filter (red line) for geopotential height z . ACCs are computed at six different forecast times (hours) at three pressure levels (rows). Four different latitudinal bands are considered (columns). The bars indicate one standard deviation.

(NCEP) Reanalysis dataset interpolated on to the SPEEDY grid. The climatology of SPEEDY is computed from the 8 year runs for the RAW filter. This follows from the fact that Amezcua *et al.* (2011) concluded there was no significant difference between the climatologies of the two filters. We select three of the seven vertical levels of the model, representing roughly the upper atmosphere (200 hPa), the middle atmosphere (510 hPa) and the lower atmosphere (835 hPa). The ACC analysis is performed for the model variables (u, v, T, q, z) in each of the aforementioned levels and is also computed for the surface variable p_s .

First, the ACC analysis is performed globally. The results for the five variables (excluding p_s) are presented in Figure 7. The ACC of the Robert–Asselin-filtered run is used as a benchmark for comparison. Therefore, this figure displays the differences $ACC_{RAW} - ACC_{RA}$ (blue lines) and $ACC_{CRAW} - ACC_{RA}$ (red lines). Amezcua *et al.* (2011) concluded that the use of the RAW filter showed a significant improvement in medium-term forecasts (72–144 h) for all variables (except q) and particularly for T and v . The conclusions for the composite RAW-filtered solutions are a little different. First of all, we notice that there is considerably more variability for the medium-term lead times.

This can be noticed from the length of the error bars for 96–144 h forecasts. Nonetheless, for short lead times (24–72 h forecasts) we observe improvement with respect to the Robert–Asselin-filtered solution for u, T and z . This last variable benefits particularly at all vertical levels. Moreover, the improvements with respect to the Robert–Asselin filter are rather more substantial than the largest improvements obtained using the RAW filter.

Now we examine regional differences. For this purpose, we perform the ACC analysis for three latitudinal bands: the Tropics (25°S to 25°N), the Northern Hemisphere midlatitudes (25°N to 75°N) and the Southern Hemisphere midlatitudes (75°S to 25°S). We have selected two variables: geopotential height z (Figure 8) and zonal wind u (Figure 9). For z , we notice significant improvements globally for all lead times from 24 to 96 h. The largest improvement comes from the Tropics at all vertical levels, although the difference with respect to RAW is particularly noticeable at 200 hPa. Also, notice that the vertical scale for this region is different from the others.

For the extratropics (both Northern and Southern Hemisphere), significant improvements are obtained at 24, 48 and 72 h. In the Northern Hemisphere this is particularly noticeable

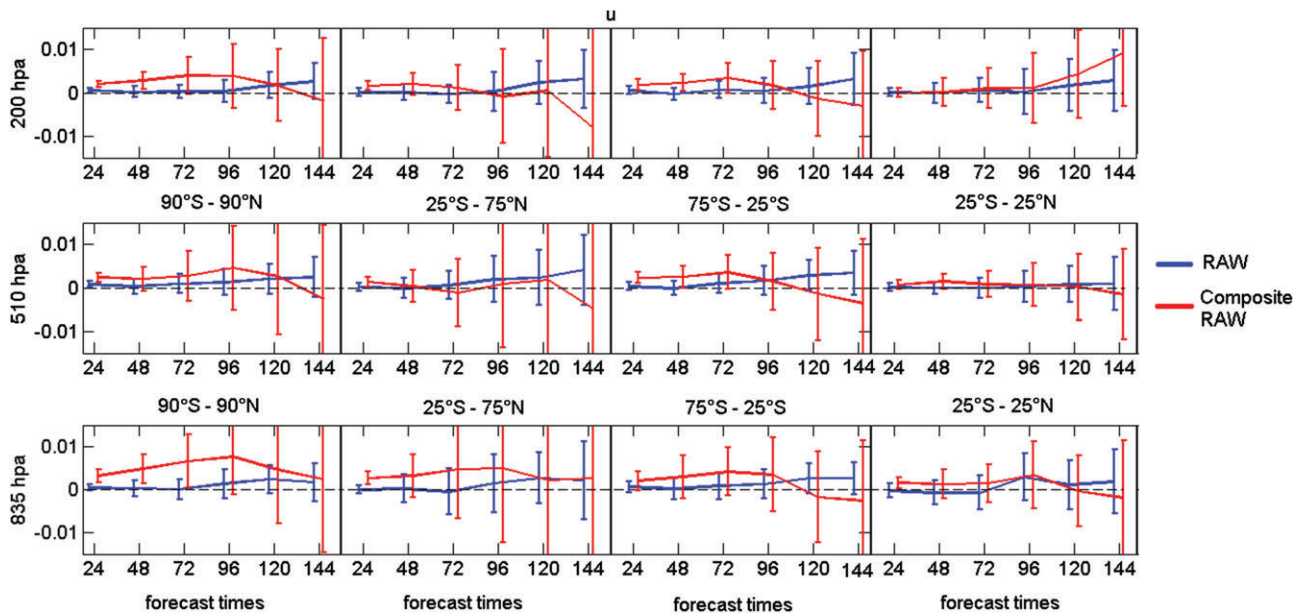


Figure 9. Anomaly correlation coefficient difference with respect to the Robert–Asselin filter for the original RAW filter (blue line) and the composite-tendency RAW filter (red line) for zonal wind u . ACCs are computed for six different forecast times (hours) at three pressure levels (rows). Four different latitudinal bands are considered (columns). The bars indicate one standard deviation.

at 200 hPa and in the Southern Hemisphere at 850 hPa. For longer lead times, the performance of RAW is better than that of composite RAW, although the long error bars of composite RAW suggest large variability in the performance of the scheme. In the case of u , the largest improvements come from the extratropics. The Northern Hemisphere seems to benefit at 24 and 48 h, while the Southern Hemisphere shows improvement in 24, 48 and 72 h forecasts at all vertical levels. There is a slight improvement in the 24 and 48 h forecasts in the Tropics in the two lower vertical levels.

5. Summary and conclusions

This article has applied the composite-tendency RAW-filtered leap-frog scheme to semi-implicit integrations. First, a theoretical analysis showed that stability and accuracy are unaffected by the introduction of the implicitly treated mode. Then the scheme was tested in semi-implicit numerical integrations in a simple nonlinear stiff system and a medium-complexity atmospheric general circulation model and was found to yield substantial improvements in both cases. We conclude that the composite-tendency RAW-filtered leap-frog scheme is suitable for use in semi-implicit integrations.

There is a time burden associated with modifying any time integration scheme. The burden is twofold, consisting of the human effort required to edit the source code as well as the possible increase in the computational expense of running the model. Based on our experience in this article, upgrading an existing semi-implicit code to include the use of a composite tendency for the explicit term is not difficult. In our experiments with SPEEDY, the update required a minor modification in one line of code in the numerical integration file. It is worth noting that our implementation of SPEEDY had already been upgraded from RA to RAW filter in the past (Amezcua *et al.*, 2011) and that this modification was also short and straightforward.

Regarding the computational expense, the method discussed in this article requires the storage of an extra field. For simple models like the elastic pendulum, in-core memory can be used for this purpose. For larger models, however, holding the extra field in memory is not feasible and the field has to be written to out-of-core memory (disc) and read in again during the next time step. There is therefore an additional input/output expense. Moreover, the method requires computing the tendency term twice and this implies an increase in the computer time employed

in the integration routine. In the case of the elastic pendulum, the computational expense increased by 18%, but it translated into a less dissipative scheme (Figure 4) and a more accurate solution (Figures 5 and 6).

In the case of SPEEDY, there was an increase in computational expense of 65%, associated with computing the tendency twice as well as writing and reading from disc. Nonetheless, considerable improvements were found in the 24–72 h forecasts. For some variables, particularly geopotential height, we found that these improvements were larger than any of the improvements brought by the use of the RAW filter alone. An interesting option would be to implement the even more accurate $(1, -4, 6, -4, 1)$ (Williams, 2013) in SPEEDY; we leave this possibility for future work. Although SPEEDY is of course only a medium-complexity general circulation model, the authors believe there are no fundamental barriers to applying the same scheme considered herein to more complicated models, for both operational numerical weather prediction and climate simulation.

Acknowledgements

JA acknowledges support from the Natural Environment Research Council (NE/I0125484/1). PDW acknowledges support via a University Research Fellowship from the Royal Society (UF080256). The authors acknowledge the useful input from Sajal Kar and an anonymous reviewer, which helped to improve the clarity of the manuscript.

References

- Amezcua J, Kalnay E, Williams PD. 2011. The effects of the RAW filter on the climatology and forecast skill of the SPEEDY model. *Mon. Weather Rev.* **139**: 608–619.
- Asselin R. 1972. Frequency filter for time integrations. *Mon. Weather Rev.* **100**: 487–490.
- Bartello P. 2002. A comparison of time discretization schemes for two-timescale problems in geophysical fluid dynamics. *J. Comput. Phys.* **179**: 268–285.
- Bourke W. 1974. A multilevel spectral model. I. Formulation and hemispheric integrations. *Mon. Weather Rev.* **102**: 687–701.
- Clancy C, Pudykiewicz JA. 2013. A class of semi-implicit predictor–corrector schemes for the time integration of atmospheric models. *J. Comput. Phys.* **250**: 665–684.
- Déqué M, Cariolle D. 1986. Some destabilizing properties of the Asselin time filter. *Mon. Weather Rev.* **114**: 880–884.
- Durrant DR. 1991. The third-order Adams–Bashforth method: An attractive alternative to leap-frog time differencing. *Mon. Weather Rev.* **119**: 702–720.
- Durrant DR. 1999. *Numerical Methods for Wave Equations in Geophysical Fluid Dynamics*. Springer: Berlin.

- Durrant DR, Blossey PN. 2012. Implicit–explicit multistep methods for fast–wave–slow–wave problems. *Mon. Weather Rev.* **140**: 1307–1325.
- Fraedrich K, Jansen H, Kirk E, Luksch U, Lunkeit F. 2005. The planet simulator: Towards a user friendly model. *Meteorol. Z.* **14**: 299–304.
- Griffies SM, Pacanowski RC, Schmidt M, Balaji V. 2001. Tracer conservation with an explicit free surface method for z-coordinate ocean models. *Mon. Weather Rev.* **129**: 1081–1098.
- Hartogh P, Medvedev AS, Kuroda T, Saito R, Villanueva G, Feofilov AG, Kutepov AA, Berger U. 2005. Description and climatology of a new general circulation model of the Martian atmosphere. *J. Geophys. Res.* **110**: E11008.
- Heimsund B-O, Berntsen J. 2004. On a class of ocean model instabilities that may occur when applying small time steps, implicit methods, and low viscosities. *Ocean Modell.* **7**: 135–144.
- Huang RX, Pedlosky J. 2003. On aliasing Rossby waves induced by asynchronous time stepping. *Ocean Modell.* **5**: 65–76.
- Kalnay E, Kanamitsu M, Kistler R, Collins W, Deaven D, Gandin L, Iredell M, Saha S, White G, Woollen J, Zhu Y, Leetmaa A, Reynolds R, Chelliah M, Ebisuzaki W, Higgins W, Janowiak J, Mo K, Ropelewski C. 1996. The NCEP–NCAR 40-year reanalysis project. *Bull. Am. Meteorol. Soc.* **77**: 437–471.
- Kantha L, Clayson C. 2000. *Numerical Models of Oceans and Oceanic Processes*, International Geophysics **66**. Academic Press: New York, NY.
- Lynch P. 2002. The swinging spring: A simple model of atmospheric balance. In *Large-Scale Atmosphere-Ocean Dynamics II: Geometric Methods and Models*, Norbury J, Roulstone I. (eds.): 64–108. Cambridge University Press: Cambridge, UK.
- Moustaoui M, Mahalov A, Kostelich EJ. 2014. A numerical method based on leap-frog and a fourth-order implicit time filter. *Mon. Weather Rev.*, doi: 10.1175/MWR-D-13-00073.1.
- Mishra SK, Srinivasan J, Nanjundiah RS. 2008. The impact of the time step on the intensity of ITCZ in an aquaplanet GCM. *Mon. Weather Rev.* **136**: 4077–4091.
- Miyoshi T. 2005. 'Ensemble Kalman filter experiments with a primitive-equation global model', PhD thesis. University of Maryland: College Park, MD.
- Molteni F. 2003. Atmospheric simulations using a GCM with simplified parametrizations. I: Model climatology and variability in multi-decadal experiments. *Clim. Dyn.* **20**: 175–191.
- Pfeffer R, Navon I, Zou X. 1992. A comparison of the impact of two time-differencing schemes on the NASA GLAS climate model. *Mon. Weather Rev.* **120**: 1381–1393.
- Robert AJ. 1996. The integration of a low order spectral form of the primitive meteorological equations. *J. Meteorol. Soc. Jpn.* **44**: 237–245.
- Teixeira J, Reynolds CA, Judd K. 2007. Time step sensitivity of nonlinear atmospheric models: Numerical convergence, truncation error growth, and ensemble design. *J. Atmos. Sci.* **64**: 175–189.
- Williams PD. 2009. A proposed modification to the Robert–Asselin time filter. *Mon. Weather Rev.* **137**: 2538–2546.
- Williams PD. 2011. The RAW filter: An improvement to the Robert–Asselin filter in semi-implicit integrations. *Mon. Weather Rev.* **139**: 1996–2007.
- Williams PD. 2013. Achieving seventh-order amplitude accuracy in leap-frog integrations. *Mon. Weather Rev.* **141**: 3037–3051.
- Williams PD, Haine TWN, Read PL, Lewis SR, Yamazaki YH. 2009. QUAGMIRE v1.3: A quasi-geostrophic model for investigating rotating fluids experiments. *Geosci. Model Dev.* **2**: 13–32.
- Williamson D. 1983. 'Description of NCAR Community Climate Model (CCMOB)', NCAR Technical Note NCAR/TN-210+STR. National Center for Atmospheric Research: Boulder, CO.
- Williamson D, Olson J. 2003. Dependence of aqua-planet simulations on time step. *Q. J. R. Meteorol. Soc.* **129**: 2049–2064.
- Zhao B, Zhong Q. 2009. The dynamical and climate tests of an atmospheric general circulation model using the second-order Adams–Bashforth method. *Acta Meteorol. Sin.* **23**: 738–749.